INTERNATIONAL JOURNAL FOR NUMERICAL METHODS IN FLUIDS, VOL. 13, 437–464 (1991)

A NUMERICAL METHOD FOR SUBCRITICAL AND SUPERCRITICAL OPEN CHANNEL FLOW CALCULATION

JOHANNES VASSILIOU SOULIS

Fluid Mechanics/Hydraulics Division, Civil Engineering Department, Demokrition University of Thrace, Xanthi 67100, Greece

SUMMARY

A marching finite volume method is presented for the calculation of two-dimensional, subcritical and supercritical, steady open channel flow including the usually neglected terms of slope and bottom friction. The channel flow will be assumed to be homogeneous, incompressible, two-dimensional and viscous with wind and Coriolis forces neglected. A hydrostatic pressure distribution is assumed throughout the flow field. The numerical technique used is a combination of the finite element and finite difference methods. A transformation is introduced through which quadrilaterals in the physical domain are mapped into squares in the computational domain. The governing system of PDEs is thus transformed into an equivalent system applied over a square grid network. Comparisons with other numerical solutions as well as with measurements for various open channel configurations show that the proposed approach is a comparatively accurate, reliable and fast technique.

KEY WORDS Free surface flow Spillways Subcritical and supercritical steady flow Marching finite volume method

INTRODUCTION

With the improvements in computational techniques and advances in computer technology, computational fluid dynamics researchers have found more effective ways of applying computational tools in the design and analysis of open channel flows. Computational procedures require very few restrictive assumptions and can be used to treat complicated configurations.

There exists a class of open channel flow problems which can be adequately described in the context of depth-averaged, two-dimensional mathematical models. Essentially, the flow properties are assumed to be invariant along the vertical direction. These simplified representations of a three-dimensional flow are justified where turbulent mixing, due to bottom roughness, effectively generates a uniform velocity distribution over the flow depth. A further assumption of hydrostatic pressure distribution seems to be valid if the water surface is not rough; and it is the objective of the designer to create a smooth water surface.

For two-dimensional open channel flows in complex geometries it is convenient to make predictions using a non-orthogonal boundary-fitted computational mesh. The computational mesh thus formed comprises equidistantly located computational nodes. The greatest advantage of the above-mentioned transformation is the accuracy and ease of application of the various types of boundary conditions which will be required to be satisfied.

Time-marching solutions of the governing flow equations are now widely used for the analysis of compressible flows[1] as well as for open channel flow analysis.[2,3] Their main attraction is the ability to compute mixed subcritical–supercritical flows with automatic capturing of hydraulic

0271-2091/91/140437-28$14.00

Received July 1989
Revised June 1990

jumps. Thus it was decided to employ a marching finite volume technique in order to solve the flow equations using a non-orthogonal computational mesh comprised of equidistantly located computational nodes.

Simplified solutions have been presented by Ippen,[4] Rouse *et al.*[5] and others. Buseman's method of characteristics was applied by Ippen and Dawson[6] to calculate the hydraulic jumps produced in supercritical flows in channels with varying cross-sectional area. Liggett and Vasudev[7] have presented a numerical solution for 2D high-speed channel flow including the slope and bottom friction terms. Charts were presented which gave an indication of the magnitude of the departure of the improved solution from the frictionless, zero-slope solutions. Two-dimensional finite difference calculation methods have been developed by McGuirk and Rodi[8] which described the circulation region immediately downstream of a side discharge into a flowing river. Chapman and Cuo[9,10] have applied a finite difference technique to the solution of the depth-integrated equations of motion in a wide shallow rectangular channel with and without an abrupt expansion. Demuren[11] presented a two-dimensional numerical procedure, based on the GENMIX code of Spalding,[12] for calculating both subcritical and supercritical flows in open channels with varying cross-section. Predictions agreed well with experimental data over a wide range of cases so long as 3D effects did not become very important. Herbich and Walsh's[13] approach is based on the method of two characteristics assuming inclined frictionless 2D flow with hydrostatic pressure distribution. Soulis and Bellos[2] presented two numerical solutions for the computation of 2D supercritical open channel flow including the friction and slope effects. The first numerical solution was obtained by using the well-known numerical scheme of MacCormack. The second solution was obtained by solving the flow equations in integral form to a series of finite volumes with adjacent volumes sharing a common face.

The predicted results were compared with other numerical solutions as well as with available measurements. The method can be utilized to eliminate the most common cause of spillway failures, namely the improper design of steep chutes.

DEFINITION OF PROBLEM

The channel flow will be assumed to be homogeneous, incompressible, two-dimensional and viscous with wind and Coriolis forces neglected. A hydrostatic pressure distribution is assumed throughout the flow field. Thus the governing flow equations for the physical domain, where the Cartesian co-ordinate system is introduced, are

$$-\frac{\partial h}{\partial t}=\frac{\partial(hu)}{\partial x}+\frac{\partial(hv)}{\partial y}, \tag{1}$$

$$-\frac{\partial(hu)}{\partial t}=\frac{\partial(gh^2/2+hu^2)}{\partial x}+\frac{\partial(huv)}{\partial y}-gh(S_{ox}-S_{fx}), \tag{2}$$

$$-\frac{\partial(hv)}{\partial t}=\frac{\partial(huv)}{\partial x}+\frac{\partial(gh^2/2+hv^2)}{\partial y}-gh(S_{oy}-S_{fy}). \tag{3}$$

Here x and y represent the Cartesian co-ordinate positions in the longitudinal and transverse directions respectively; t is the time; u and v are the averaged velocity components in the x- and y-directions respectively; h is the water depth; g is the acceleration due to gravity; S_{ox} and S_{oy} are the channel slopes defined as

$$S_{ox} = -\frac{\partial z_o}{\partial x}, \tag{4}$$

$$S_{oy} = -\frac{\partial z_o}{\partial y}, \tag{5}$$

where z_o is the bottom elevation; and the friction slopes in the x- and y-directions are defined as

$$S_{fx} = \frac{u\sqrt{(u^2+v^2)}}{hc^2}, \tag{6}$$

$$S_{fy} = \frac{v\sqrt{(u^2+v^2)}}{hc^2}, \tag{7}$$

where C is Chézy's flow friction coefficient. Another option calculates the friction slopes using Manning's friction coefficient n. In this case the friction slopes are

$$S_{fx} = \frac{n^2 u\sqrt{(u^2+v^2)}}{h^{4/3}}, \tag{8}$$

$$S_{fy} = \frac{n^2 v\sqrt{(u^2+v^2)}}{h^{4/3}}. \tag{9}$$

By writing the equation for frictional resistance in this way, it was assumed that all of the resistance is due to bottom friction, thus neglecting the boundary layers on the side walls. The depth-integrated effective stress has been neglected in order to eliminate the possibility of introducing numerical smoothing. The time derivative terms in the flow equations should not be misinterpreted as an attempt to solve unsteady flow phenomena; they are simply a convenient way to iterate to a steady-state solution (time-marching method).

TRANSFORMATION OF THE FLOW EQUATIONS

The essence of the proposed marching finite volume scheme is that distorted squares in the physical domain will be separately mapped into squares in the computational domain by independent transformations from Cartesian (x, y) to local (ξ, η) co-ordinates (Figure 1). A finite volume (cell) which is a quadrilateral in the physical plane or just a square in the computational plane is formed by four nodes (linear element) located at the four corners of the element. The quadrilaterals are packed around the boundaries of the hydraulic structure and cover the whole flow field (Figure 2).

The numerical scheme allows complete flexibility in choosing the spacing in the longitudinal and transverse directions. Moreover, the transversewise lines shown in Figure 2 can take any possible direction in order to accommodate abrupt changes of the hydraulic structure geometry. However, all current method applications utilize a computational grid similar to that shown in Figure 2, which is the most common choice in channel flow calculations. Such grid structures require minimal programming effort.

If x_i, y_i $(i=1, 2, 3, 4)$ are the Cartesian co-ordinates of a finite volume, then the co-ordinates of any point of this element can be expressed as

$$x = \sum_1^4 x_i N_i, \qquad y = \sum_1^4 y_i N_i, \tag{10}$$

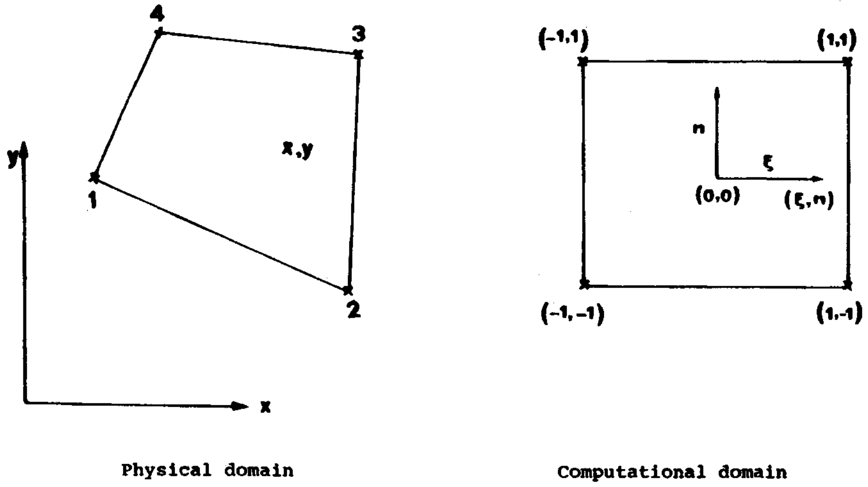

Physical domain Computational domain

Figure 1. Distorted squares mapped into squares

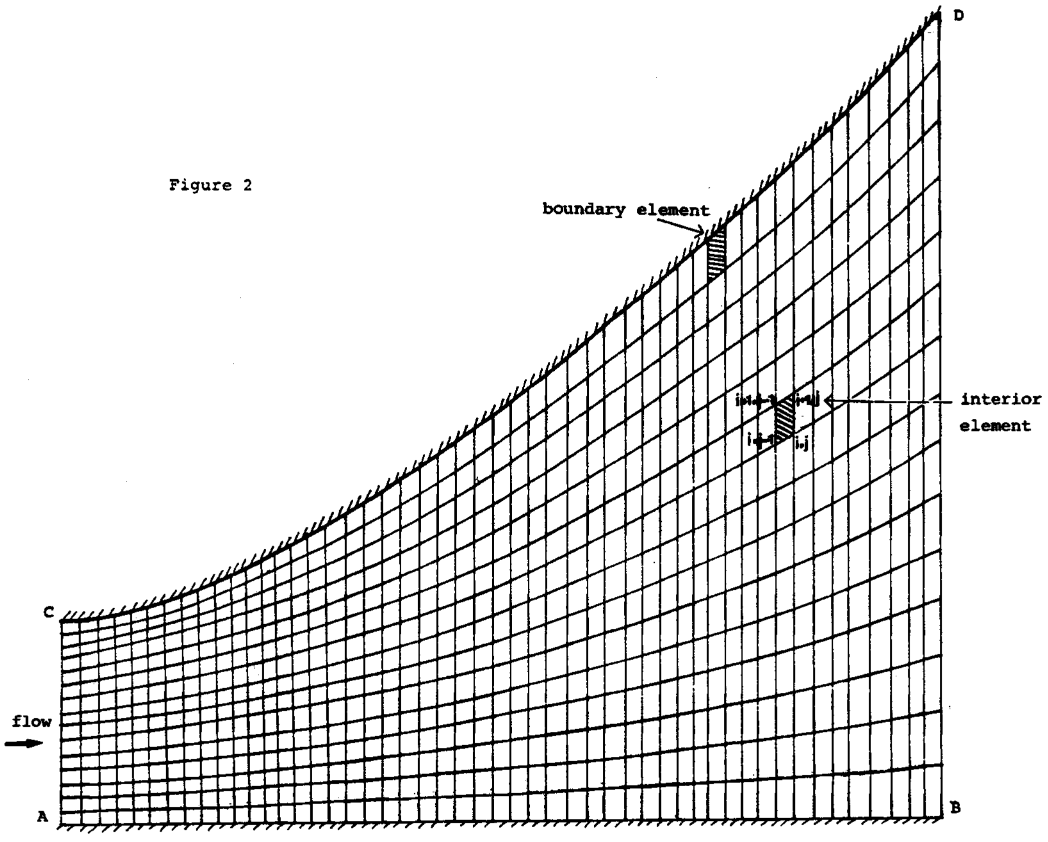

Figure 2. Typical computational grid and finite volume elements

where N_i are the shape functions associated with the finite volume nodes. The shape functions are defined in terms of the local non-orthogonal co-ordinate system as

$$
\begin{aligned}
N_1&=(1-\xi)(1-\eta)/4, \qquad & N_2&=(1+\xi)(1-\eta)/4,\\
N_3&=(1+\xi)(1+\eta)/4, \qquad & N_4&=(1-\xi)(1+\eta)/4.
\end{aligned}
\tag{11}
$$

The local co-ordinates lie in the range $-1\leqslant\xi\leqslant 1$, $-1\leqslant\eta\leqslant 1$ so that vertices of the square are at $\xi=\pm 1, \eta=\pm 1$.

Let $[J^{-1}]$ be the transformation matrix from the physical to the local co-ordinate system:

$$
[J^{-1}]=\begin{bmatrix} \partial x/\partial\xi & \partial x/\partial\eta \\ \partial y/\partial\xi & \partial y/\partial\eta \end{bmatrix}.
\tag{12}
$$

The following relations hold:[14]

$$
\begin{aligned}
\frac{\partial x}{\partial \xi}&=J^{-1}\frac{\partial \eta}{\partial y}, \qquad & \frac{\partial x}{\partial \eta}&=-J^{-1}\frac{\partial \xi}{\partial y},\\
\frac{\partial y}{\partial \xi}&=-J^{-1}\frac{\partial \eta}{\partial x}, \qquad & \frac{\partial y}{\partial \eta}&=J^{-1}\frac{\partial \xi}{\partial x},
\end{aligned}
\tag{13}
$$

where J^{-1} is the determinant of matrix $[J^{-1}]$. Under the aformentioned transformation of equations (1)–(3) into the local co-ordinate system (ξ, η) they assume the form[15,16]

$$
\frac{\partial(J^{-1}h)}{\partial t}+\frac{\partial(J^{-1}hU)}{\partial \xi}+\frac{\partial(J^{-1}hV)}{\partial \eta}=0,
\tag{14}
$$

$$
\frac{\partial(J^{-1}hu)}{\partial t}+\frac{\partial}{\partial \xi}\left[J^{-1}\left(hUu+\frac{\partial \xi}{\partial x}\frac{gh^2}{2}\right)\right]+\frac{\partial}{\partial \eta}\left[J^{-1}\left(hVu+\frac{\partial \eta}{\partial x}\frac{gh^2}{2}\right)\right]=J^{-1}gh(S_{ox}-S_{fx}),
\tag{15}
$$

$$
\frac{\partial(J^{-1}hv)}{\partial t}+\frac{\partial}{\partial \xi}\left[J^{-1}\left(hUv+\frac{\partial \xi}{\partial y}\frac{gh^2}{2}\right)\right]+\frac{\partial}{\partial \eta}\left[J^{-1}\left(hVv+\frac{\partial \eta}{\partial y}\frac{gh^2}{2}\right)\right]=J^{-1}gh(S_{oy}-S_{fy}),
\tag{16}
$$

where U and V are the velocity components along the ξ- and η-directions respectively and the velocity components u and v in the physical domain are

$$
\begin{bmatrix} u \\ v \end{bmatrix}=[J^{-1}]\begin{bmatrix} U \\ V \end{bmatrix}.
\tag{17}
$$

NUMERICAL FORMULATION

The finite volumes (cells) used for the current numerical scheme are formed by quasi-streamlines and transverse lines where the element nodes are located at each of the four vertices (linear element). A wide range of finite elements are possible for adequate description of the surface boundaries, and minimal computational code logic is required for changing a particular element to a more sophisticated one.

For a control volume ΔV of unit height and for a given time step Δt the transformed governing

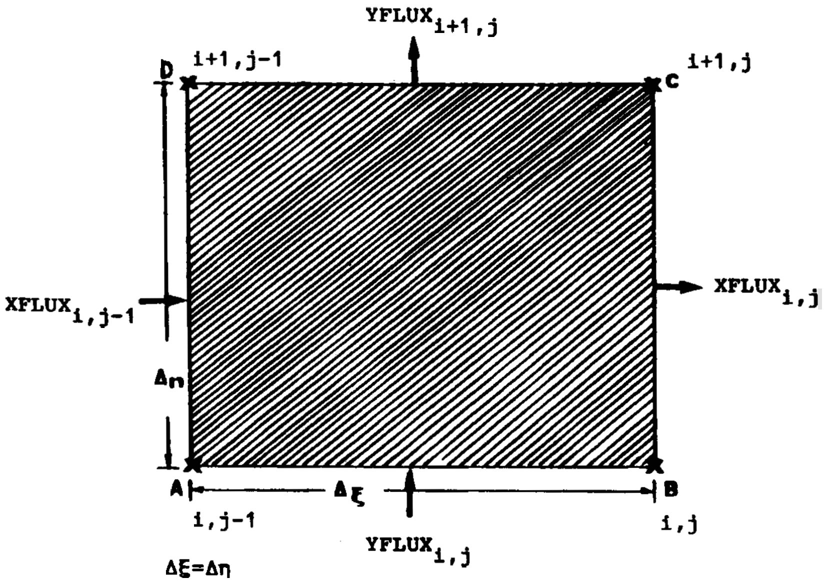

Figure 3. Flux balancing across a finite volume

flow equations (14)–(16) may be written as

$$-\Delta(J^{-1}h)=[\Delta(J^{-1}hU)\Delta\eta+\Delta(J^{-1}hV)\Delta\xi]\frac{\Delta t}{\Delta\xi\Delta\eta}, \tag{18}$$

$$-\Delta(J^{-1}hu)=\left\{\Delta\left[J^{-1}\left(hUu+\frac{\partial\xi}{\partial x}\frac{gh^2}{2}\right)\right]\Delta\eta+\Delta\left[J^{-1}\left(hVu+\frac{\partial\eta}{\partial x}\frac{gh^2}{2}\right)\right]\Delta\xi\right\}\frac{\Delta t}{\Delta\xi\Delta\eta}$$
$$-J^{-1}gh(S_{ox}-S_{fx})\Delta t, \tag{19}$$

$$-\Delta(J^{-1}hv)=\left\{\Delta\left[J^{-1}\left(hUv+\frac{\partial\xi}{\partial y}\frac{gh^2}{2}\right)\right]\Delta\eta+\Delta\left[J^{-1}\left(hVv+\frac{\partial\eta}{\partial y}\frac{gh^2}{2}\right)\right]\Delta\xi\right\}\frac{\Delta t}{\Delta\xi\Delta\eta}$$
$$-J^{-1}gh(S_{oy}-S_{fy})\Delta t. \tag{20}$$

Figure 3 shows the notation used for the flux balancing across a finite volume of the flow field. Thus for the *mass flux* an XFLUX at point i,j is defined as

$$(\text{XFLUX})_{i,j}=[(J^{-1}hU)_{i+1,j}+(J^{-1}hU)_{i,j}]\Delta\eta/2,$$

while the YFLUX at the same point i,j is defined as

$$(\text{YFLUX})_{i,j}=[(J^{-1}hV)_{i,j}+(J^{-1}hV)_{i,j-1}]\Delta\xi/2.$$

For the *x-momentum* flux balance the corresponding $(\text{XFLUX})_{i,j}$ and $(\text{YFLUX})_{i,j}$ are defined as

$$(\text{XFLUX})_{i,j}=\left\{\left[J^{-1}\left(hUu+\frac{\partial\xi}{\partial x}\frac{gh^2}{2}\right)\right]_{i+1,j}+\left[J^{-1}\left(hUu+\frac{\partial\xi}{\partial x}\frac{gh^2}{2}\right)\right]_{i,j}\right\}\frac{\Delta\eta}{2},$$

$$(\text{YFLUX})_{i,j}=\left\{\left[J^{-1}\left(hVu+\frac{\partial\eta}{\partial x}\frac{gh^2}{2}\right)\right]_{i,j}+\left[J^{-1}\left(hVu+\frac{\partial\eta}{\partial x}\frac{gh^2}{2}\right)\right]_{i,j-1}\right\}\frac{\Delta\xi}{2}.$$

Similarly, for the *y-momentum* flux balance the corresponding $(\mathrm{XFLUX})_{i,j}$ and $(\mathrm{YFLUX})_{i,j}$ are defined as

$$(\mathrm{XFLUX})_{i,j}=\left\{\left[J^{-1}\left(hUv+\frac{\partial\xi}{\partial y}\frac{gh^2}{2}\right)\right]_{i+1,j}+\left[J^{-1}\left(hUv+\frac{\partial\xi}{\partial y}\frac{gh^2}{2}\right)\right]_{i,j}\right\}\frac{\Delta\eta}{2},$$

$$(\mathrm{YFLUX})_{i,j}=\left\{\left[J^{-1}\left(hVv+\frac{\partial\eta}{\partial y}\frac{gh^2}{2}\right)\right]_{i,j}+\left[J^{-1}\left(hVv+\frac{\partial\eta}{\partial y}\frac{gh^2}{2}\right)\right]_{i,j-1}\right\}\frac{\Delta\xi}{2}.$$

The terms $\Delta(J^{-1}hU)$ and $\Delta(J^{-1}hV)$ of the RHS of equation (18) are defined as

$$\Delta(J^{-1}hU)=(\mathrm{XFLUX})_{i,j}-(\mathrm{XFLUX})_{i,j-1}, \tag{21}$$

$$\Delta(J^{-1}hV)=(\mathrm{YFLUX})_{i+1,j}-(\mathrm{YFLUX})_{i,j}. \tag{22}$$

Similar differencing is adopted for the RHS differences of equations (19) and (20). The bottom slopes S_{ox} and S_{oy} are precalculated and stored, while the friction slopes S_{fx} and S_{fy} are updated in every time step Δt.

All these fluxes may now be used in equations (18)–(20) to obtain the changes $\Delta(J^{-1}h)$, $\Delta(J^{-1}hu)$ and $\Delta(J^{-1}hv)$ and thus the values of h, u and v for the time step under consideration. In all currently presented applications the above-mentioned changes are distributed between the four corners A, B, C and D of the finite volume (Figure 3). It was decided to send half the information regarding the changes in water depth h as well as in hu and hv to the upstream face of the finite volume involved, while the other half is sent to the downstream face. This scheme was found to be suitable. The decision was made after numerical experimentation. The changes were not directly used to yield the corresponding values of h, u and v. For all test runs two different amplification factors were used: a C_1-factor for the estimation of h and a C_2-factor for the estimations of u and v. The procedure is as follows:

$$(J^{-1}h)_{i,j}^{n+1}=(J^{-1}h)_{i,j}^{n}+\frac{\Delta(J^{-1}h)_{i,j}^{n+1}}{1+|C_1\Delta(J^{-1}h)_{i,j}^{n+1}|}, \tag{23}$$

where $C_1=1{\cdot}0/h_{1,1}^{0}$;

$$(J^{-1}hu)_{i,j}^{n+1}=(J^{-1}hu)_{i,j}^{n}+\frac{\Delta(J^{-1}hu)_{i,j}^{n+1}}{1+|C_2\Delta(J^{-1}hu)_{i,j}^{n+1}|}, \tag{24}$$

where $C_2=0{\cdot}25/h_{1,1}^{0}$. The upper index n denotes the computed results of the previous iteration. A relation similar to equation (24) holds for the estimation of $(J^{-1}hv)_{i,j}^{n+1}$. The numerical scheme was found to be stable over a wide range of considered values of C_1 and C_2. Once a steady state solution is obtained, the sum of the fluxes of each conserved variable over the faces of each finite volume will be zero and hence the conservation equations are satisfied irrespective of how these changes are distributed. Table I gives the details of the iterative scheme. The order in which the x- and y-momentum equations are solved is not important. The equations must be solved in the order: continuity, momentum. During an iteration the terms $J^{-1}gh(S_{ox}-S_{fx})$ and $J^{-1}gh(S_{oy}-S_{fy})$ were relaxed before they were incorporated into the governing flow equations. A typical relaxation factor for all test runs was 0·9.

BOUNDARY CONDITIONS

For *subcritical flow entrance* the following conditions have been proved to be valid: Along the upstream boundary AC (Figure 2) a relative flow direction is specified; across the flow field of the

Table I. Outline of the marching finite volume iterative scheme

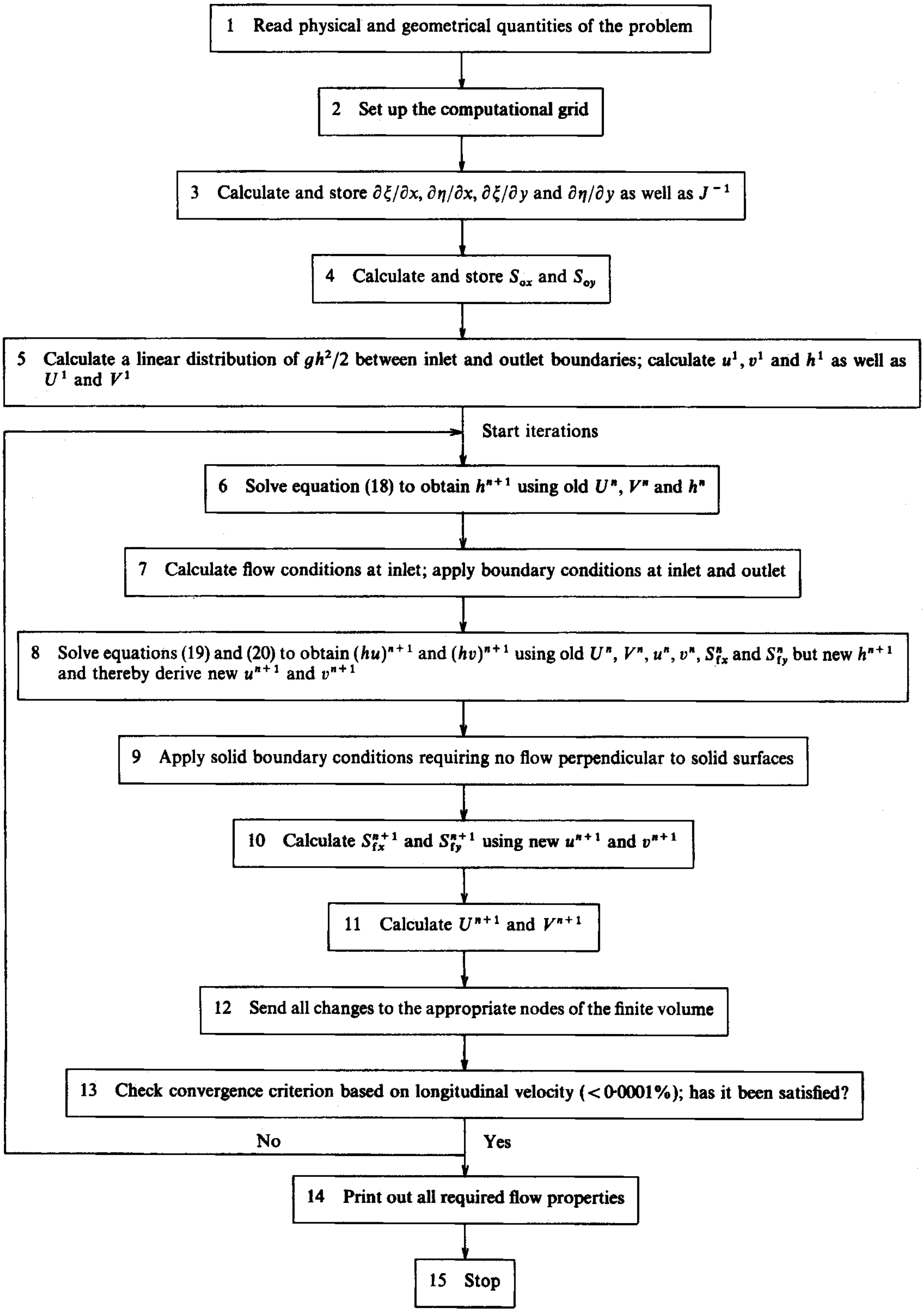

1 Read physical and geometrical quantities of the problem

2 Set up the computational grid

3 Calculate and store $\partial\xi/\partial x$, $\partial\eta/\partial x$, $\partial\xi/\partial y$ and $\partial\eta/\partial y$ as well as J^{-1}

4 Calculate and store S_{ox} and S_{oy}

5 Calculate a linear distribution of $gh^2/2$ between inlet and outlet boundaries; calculate u^1, v^1 and h^1 as well as U^1 and V^1

6 Solve equation (18) to obtain h^{n+1} using old U^n, V^n and h^n

7 Calculate flow conditions at inlet; apply boundary conditions at inlet and outlet

8 Solve equations (19) and (20) to obtain $(hu)^{n+1}$ and $(hv)^{n+1}$ using old U^n, V^n, u^n, v^n, S^n_{fx} and S^n_{fy} but new h^{n+1} and thereby derive new u^{n+1} and v^{n+1}

9 Apply solid boundary conditions requiring no flow perpendicular to solid surfaces

10 Calculate S^{n+1}_{fx} and S^{n+1}_{fy} using new u^{n+1} and v^{n+1}

11 Calculate U^{n+1} and V^{n+1}

12 Send all changes to the appropriate nodes of the finite volume

13 Check convergence criterion based on longitudinal velocity ($< 0.0001\%$); has it been satisfied?

14 Print out all required flow properties

15 Stop

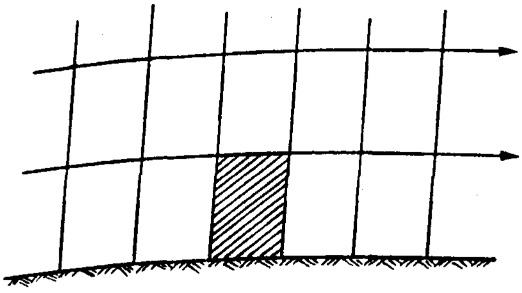

Figure 4. Solid boundary finite volume for the first computational row ($i=1, j=1, JM$)

hydraulic structure a fixed value for the flow rate Q is also specified. At the downstream boundary BD a specified uniform-across-the-width water depth is assumed. In cases where a mixed subcritical–supercritical type of flow is to be encountered (always subcritical flow entrance) a value for the upstream total head is specified instead of the flow rate. However, this test is not reported in the current work.

For *supercritical flow entrance* the following conditions have been proved to be valid. Along the upstream boundary AC (Figure 2) the transverse flow direction velocity component is specified; a uniform-across-the-width water depth is also specified along with the total available head H_{01}. In cases where hydraulic jumps are to be encountered the downstream water depth h_2 needs to be specified.

To close the problem, the condition of no mass flow across the *solid boundaries* needs to be applied. The fluxes hu and hv are taken across the faces of the boundary finite volume (Figures 2 and 4) which are bounded by the body surface. Thereafter the flux components hu and hv for the solid boundaries are recalculated requiring the velocity component normal to the solid face to be zero.

NUMERICAL RESOLUTION

Iterations were continued until the maximum change of longitudinal velocity component between successive iterations dropped below 0·0001%. The total number of iterations required to achieve convergence was about 700, depending upon the geometrical complexity, initial water depth distribution and type of flow (subcritical–supercritical) (Figure 5). Subcritical flow problems proved to be slower in achieving convergence compared to supercritical ones. The computational grid was formed by finite volumes of $\Delta x:\Delta y \simeq 1:1$. Typical test modellings have been carried out using a mesh of 15 × 60 grid points (Rouse *et al.*[5] expansion channel at $Fr_1 = 4{\cdot}0$). Grid reduction tests for the above channel have shown (Figure 6) that the $\Delta x:\Delta y$ ratio above a certain value does not essentially alter the depth distribution (maximum errors of less than 1·0%).

As with all times-marching methods, the theoretical maximum stable time step Δt is determined by the CFL criterion

$$\Delta t = \frac{\Delta x}{u + \sqrt{(gh)}}, \tag{25}$$

where Δx is the streamwise distance between the upstream and downstream faces of a finite volume. Usually, instead of Δx, a distance $\Delta x_{\min}$ was used. $\Delta x_{\min}$ is calculated as the minimum value of all Δxs of the utilized grid. In practice the above-calculated Δt was multiplied by C_3,

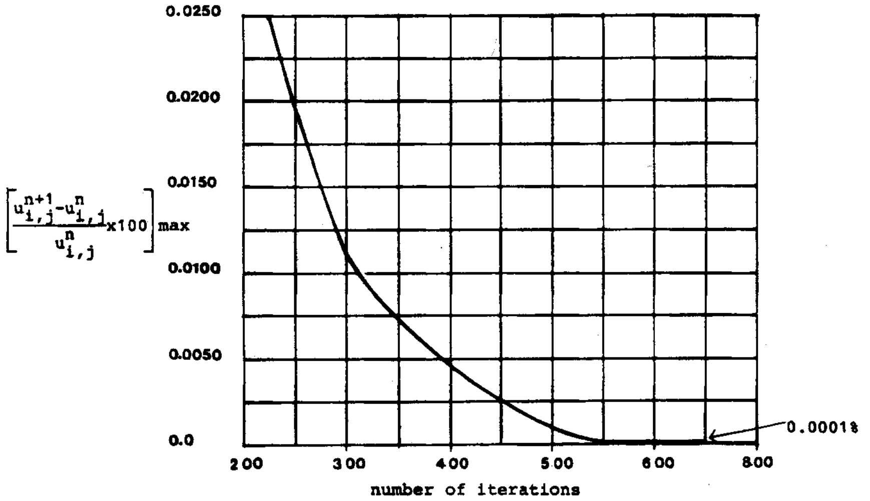

Figure 5. Convergence history for the Rouse *et al.* expansion channel at $Fr_1 = 4{\cdot}0$

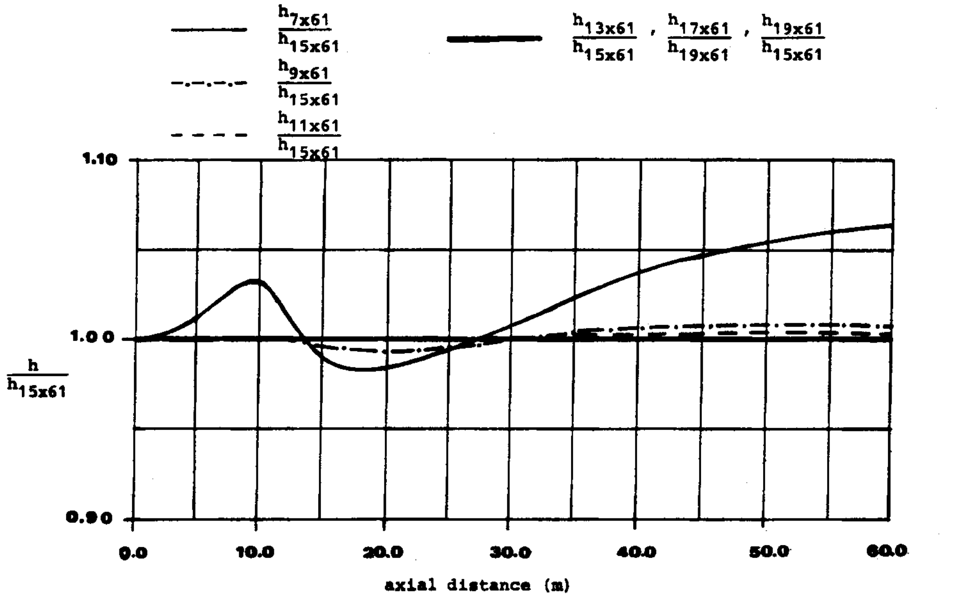

Figure 6. Grid reduction tests for the Rouse *et al.* expansion channel at $Fr_1 = 4{\cdot}0$

a time factor, so as to achieve convergence. In order to speed up the solution, the value of C_3 used was determined by numerical experimentation. Numerical instability can arise from improper selection of $\Delta x{:}\Delta y$ ratios. Therefore some extra numerical experimentation is needed.

Many other forms of discrete approximation of the partial differential equations could have been selected by altering the order of the finite element involved. With the current code, sufficient flexibility exists for special regions of the mesh where resolution is otherwise inadequate due to steep gradients in the dependent variable.

All current test runs have been carried out on a Micro Vax II computer.

APPLICATIONS

Subcritical flow in a straight parallel wall channel

The first flow test is a subcritical flow in a straight parallel wall channel of rectangular cross-section. The problem selected is a flow rate of 20·0 $\mathrm{m^3\,s^{-1}}$ with an average exit depth of 2·0 m and an inlet zero flow angle. The channel width is 7·0 m while the total length of the hydraulic structure is 14·0 m. In order to get an indication of the computed results, it was decided to employ a standard quasi-2D fixed-step numerical method. The water depth profiles are computed in the form

$$h_{i+1}=h_i+(S_o-S_f)(x_{i+1}-x_i)-\frac{u_{i+1}^2}{2g}+\frac{u_i^2}{2g}. \tag{26}$$

A definition sketch is shown in Figure 7. In performing the numerical integration the $\Delta x=x_{i+1}-x_i$ step is held constant, S_f is evaluated using Chézy's equation, h_{i+1} = constant at $x_{i+1}=0{\cdot}0$, S_o is the bottom slope and the discharge Q is also constant. This technique enables variable-width channel flows to be calculated. Comparisons between the proposed numerical

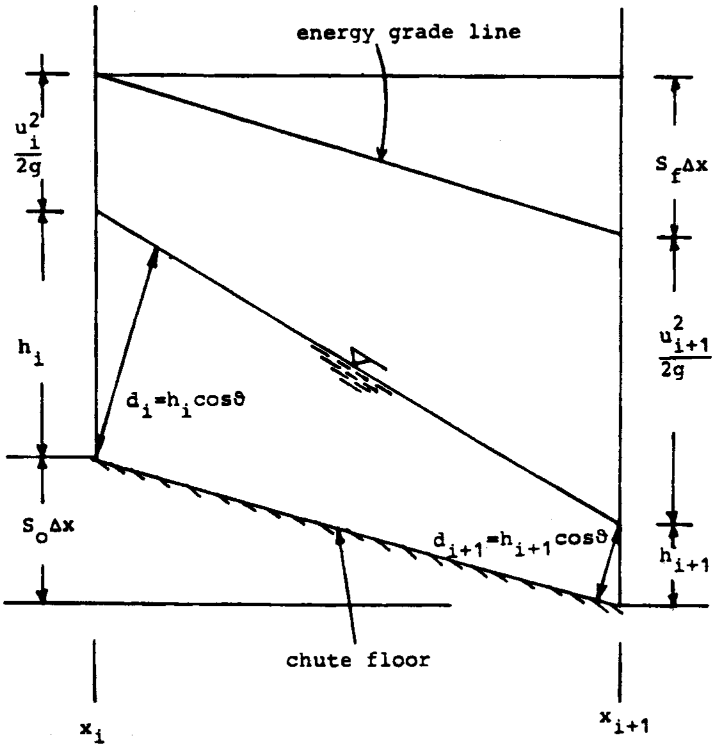

Figure 7. Definition sketch for gradually varied flow

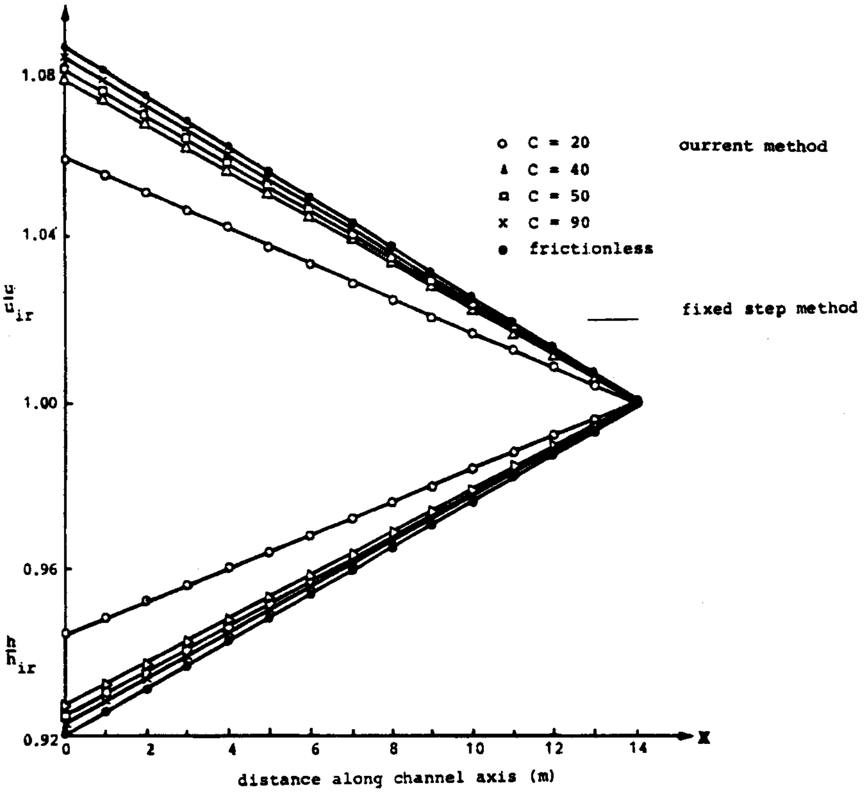

Figure 8. Comparisons between current method and fixed-step method predictions of subcritical velocity and depth distributions for straight parallel wall channel geometry at $Q = 20{\cdot}0$ m^3 s^{-1}, $h_2 = 2{\cdot}0$ m and $S_{ox} = 0.01$ using various Chézy friction coefficients

method results and the above-described standard fixed-step method predictions for velocity and water depth distributions are shown in Figure 8. Actually, this figure shows the centreline velocities and water depths as compared to the frictionless zero-slope solution denoted by the subscript 'ir' (irrotational flow). It must be emphasized that the velocity throughout the flow field is subcritical ($Fr = u/\sqrt{(gh)} < 1{\cdot}0$). The utilized Chézy flow friction coefficients range from $C = 20{\cdot}0$ to frictionless flow, while S_{ox} is set equal to 0·01. The comparison is satisfactory. Figure 9 shows the bottom slope effects at $C = 50{\cdot}0$ for the above-mentioned flow conditions. The comparison is again satisfactory.

Convex chute in converging supercritical flow

Steep chutes are commonly used in hydraulic structures as conveyances for high-velocity (supercritical) flows between a spillway crest and an energy dissipator. Whenever the crest length is greater than the width of the energy dissipator, the chute must converge in the downstream direction. Neilson[17] studied the shape in plan of the chute side walls; the object was to study the relationships commonly used to design an acceptable rate of curvature of the side walls. He set up an experimental rig. Figure 10 shows the details of the profile of the spillway downstream from the crest. The slope of the chute was 0·1799:1 (equalling 10·2°). The total length of the crest was 0·762 m. A definition sketch for the convergence geometry is shown in Figure 11.

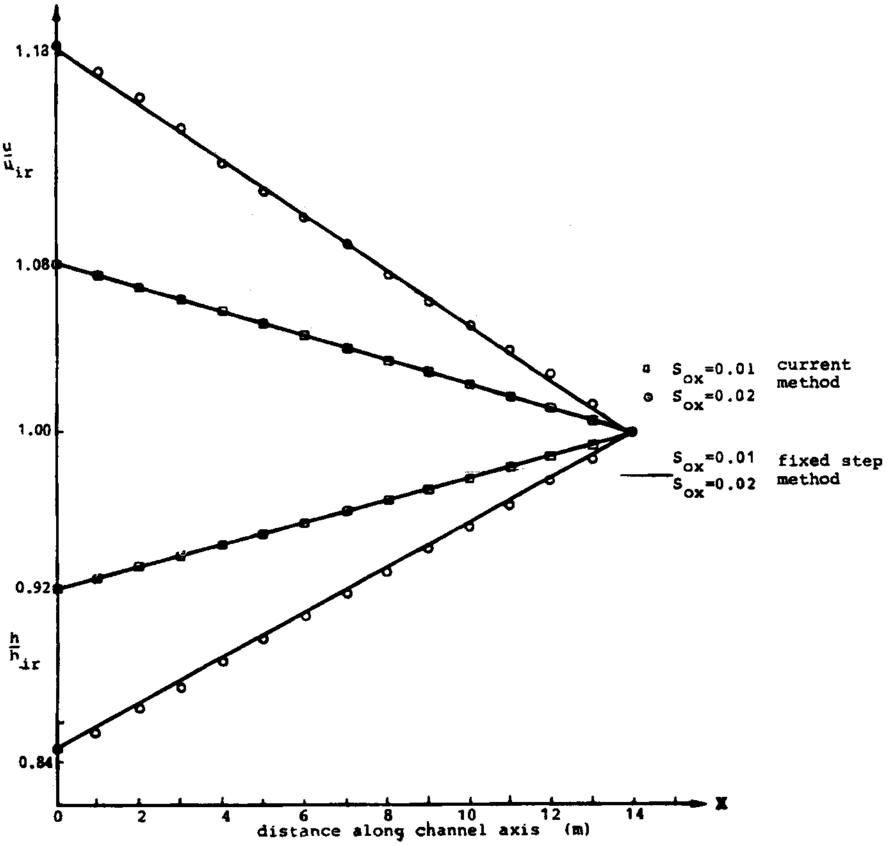

Figure 9. Comparison between current method and fixed-step method predictions of subcritical velocity and depth distributions for straight parallel wall geometry at $Q=20\cdot0\ \mathrm{m^3\,s^{-1}}$, $h_2=2\cdot0$ m and $C=50$ using various slopes

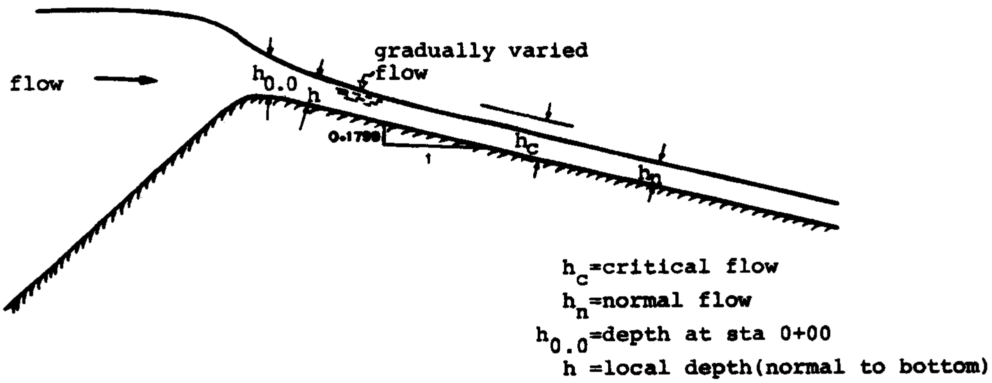

Figure 10. General flow profile

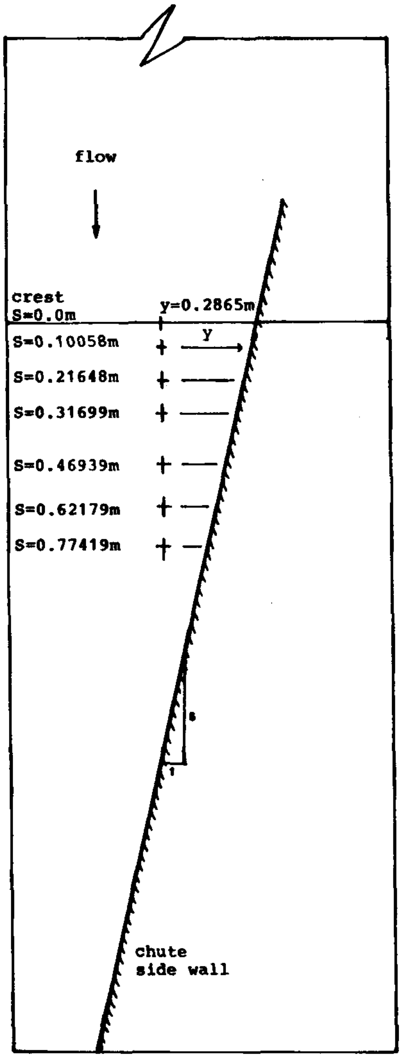

Figure 11. Definition sketch for the convergence geometry of Neilson's convex chute

The side wall chute is inclined 5:1. The total length (axial distance) of the chute was 2·469 m. A value for the Manning flow friction coefficient n was obtained equal to 0·012, which agrees with published values for a planed wood surface. This value was used in all subsequent computations herein. Three test runs were reported by Nielson in order to determine the water surface cross-section profiles. The first test run used $Q=0{\cdot}0167\ \mathrm{m^3\,s^{-1}}$, the second $Q=0{\cdot}02803\ \mathrm{m^3\,s^{-1}}$ and the third $Q=0{\cdot}0419\ \mathrm{m^3\,s^{-1}}$ (which was used to test a converging–diverging chute). The current numerical method was used to predict the water surface cross-sections for the first two discharges. Figures 12(a)–12(c) show the comparison between the predicted and measured[17] water surface cross-section profiles for the $Q=0{\cdot}0167\ \mathrm{m^3\,s^{-1}}$ test case. The critical depth for the lower-discharge case is 0·0369 m. The comparison is considered to be satisfactory for nearly all stations. Figures 13(a)–13(c) show the comparison between measurements and predictions for the

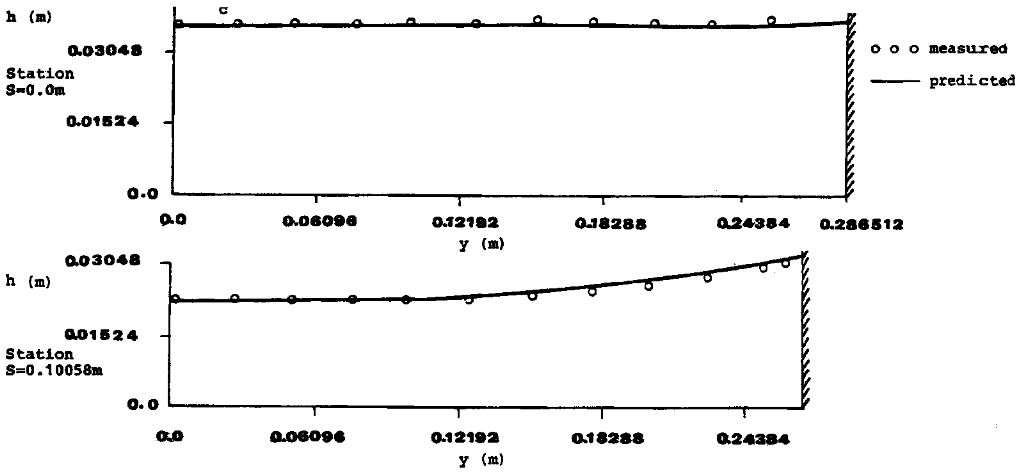

Figure 12(a). Water surface cross-section profiles for the $Q = 0{\cdot}0167\ \mathrm{m}^3\,\mathrm{s}^{-1}$ test case at stations 0·0 and 0·1006 m

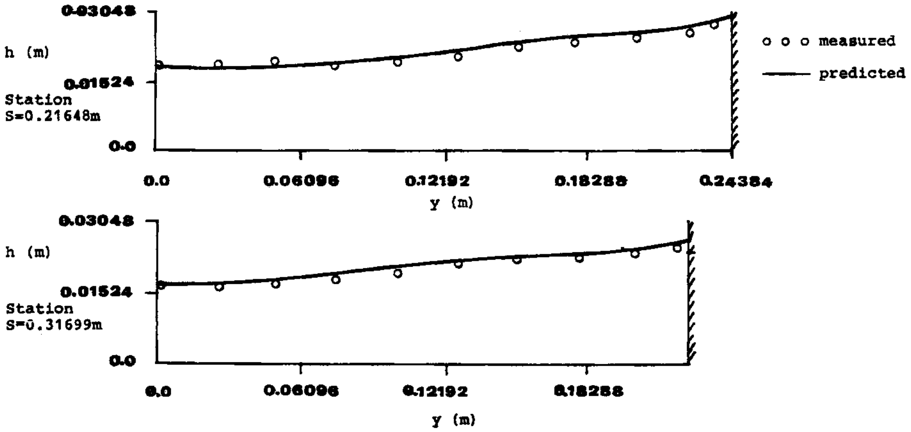

Figure 12(b). Water surface cross-section profiles for the $Q = 0{\cdot}0167\ \mathrm{m}^3\,\mathrm{s}^{-1}$ test case at stations 0·2164 and 0·3170 m

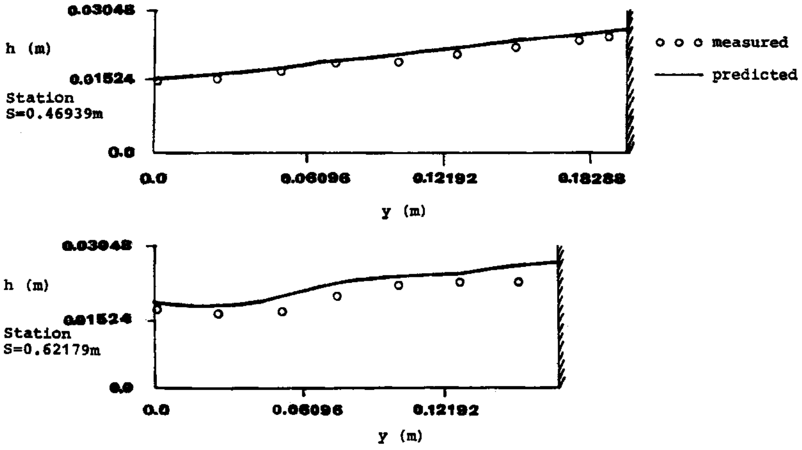

Figure 12(c). Water surface cross-section profiles for the $Q = 0{\cdot}0167\ \mathrm{m}^3\,\mathrm{s}^{-1}$ test case at stations 0·4694 and 0·6218 m

$Q=0{\cdot}02803\ \mathrm{m^3\,s^{-1}}$ test case. Here the critical depth value is 0·0521 m. Again the agreement is satisfactory, although at the downstream stations (Figure 13(c)) the predictions tend to yield higher water depth values than the measured ones. Close to the side walls the water depth values (measured and predicted) are higher than those of the main flow regions.

Linearly expanding channel

The channel transition shown in Figure 14 was used to test the numerical solution for an expanding channel with supercritical flow. The length of the expansion is 11 *b*, where *b* is the half-

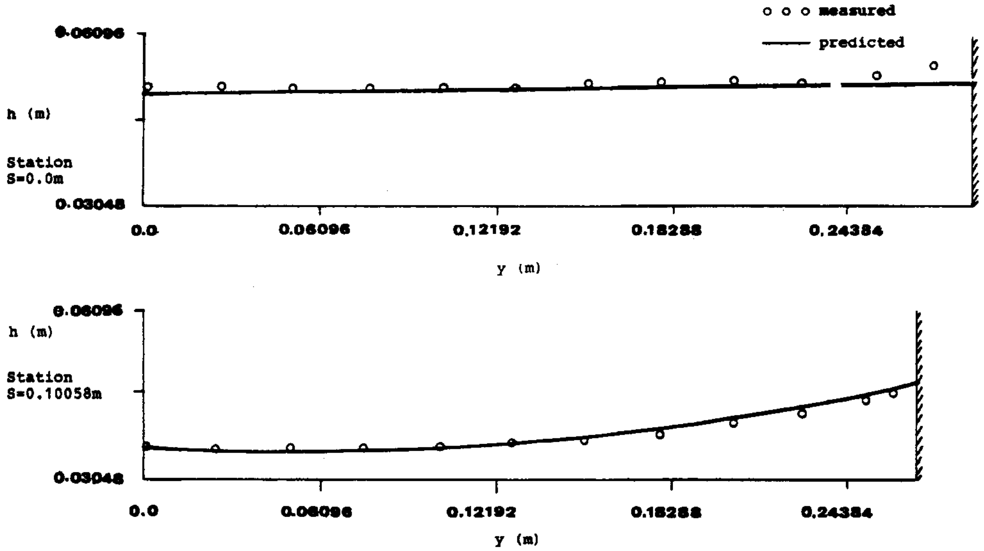

Figure 13(a). Water surface cross-section profiles for the $Q=0{\cdot}02803\ \mathrm{m^3\,s^{-1}}$ test case at stations 0·0 and 0·1006 m

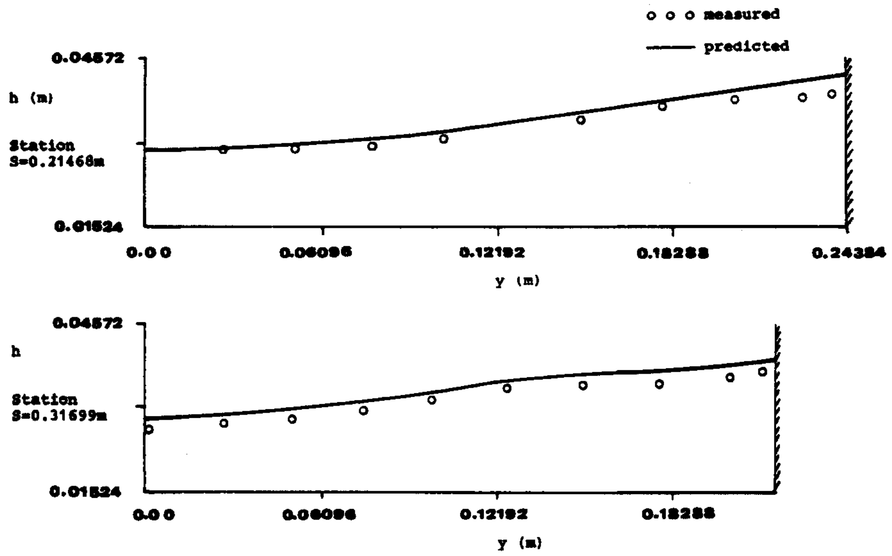

Figure 13(b). Water surface cross-section profiles for the $Q=0{\cdot}02803\ \mathrm{m^3\,s^{-1}}$ test case at stations 0·2164 and 0·3170 m

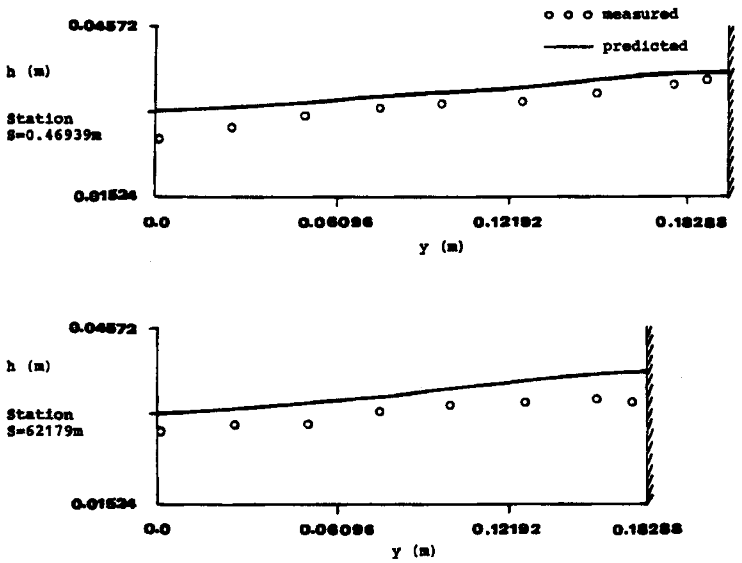

Figure 13(c). Water surface cross-section profiles for the $Q=0{\cdot}02803\ \mathrm{m^3\,s^{-1}}$ test case at stations 0·4694 and 0·6218 m

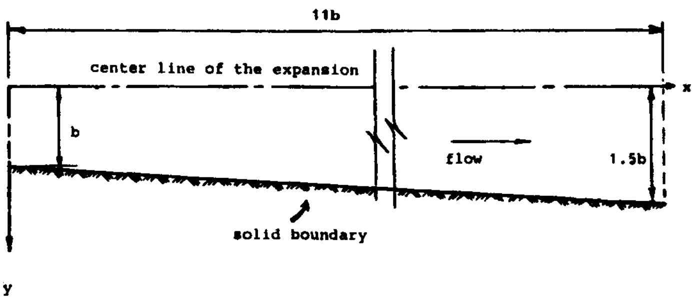

Figure 14. Linearly expanding channel geometry

entrance width, and the final width is 1·5*b*. The expansion was tested for an entrance Froude number of 2·0 and a depth-to-width ratio h/b at entrance of 0·5.

Figure 15 shows the variation of the centreline velocities in the improved solution as compared to the frictionless, zero-slope solution (denoted by 'ir') for a flat slope. Identical flow behaviour has been derived using the integral method.[2]

Figure 16 shows the predictions of exit velocity variation with channel slope at $Fr_1=2{\cdot}0$ and $h/b=0{\cdot}5$ using various Chézy flow friction coefficients. For steep slopes the agreement between the current method predictions and those of the integral method worsens. Finally, Figure 17 shows the predictions of exit velocity variation with Chézy's flow friction coefficient using various channel slopes.

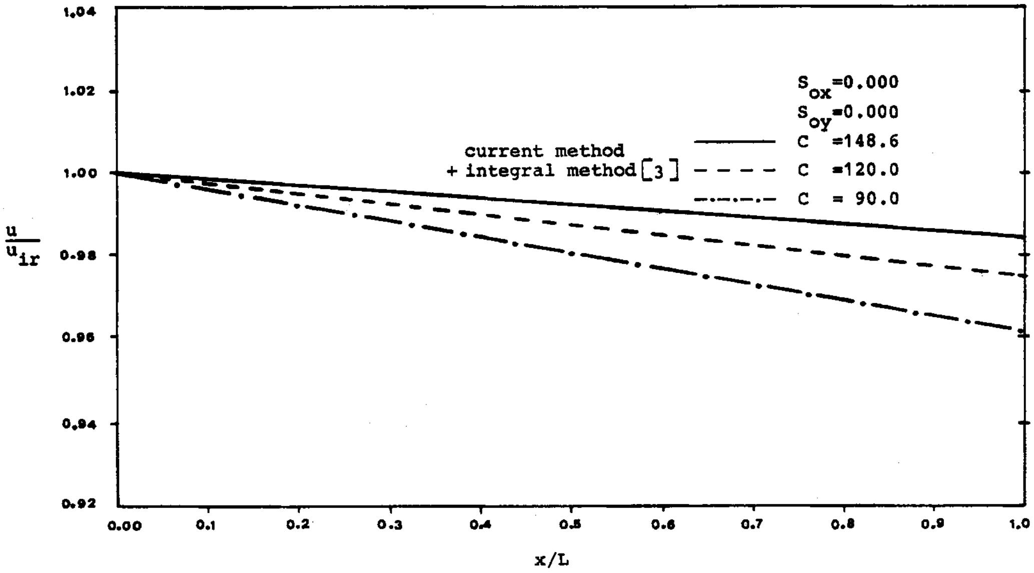

Figure 15. Predictions of the centreline velocity distributions for the linearly expanding channel at $Fr_1 = 2{\cdot}0$ using various Chézy flow friction coefficients

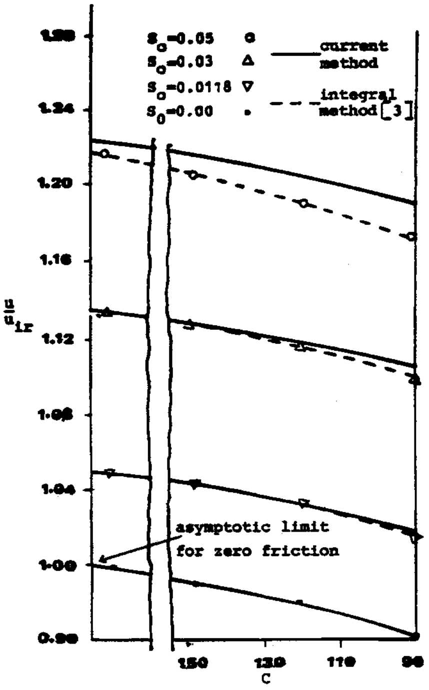

Figure 16. Predictions of exit velocity variation with channel slope for the linearly expanding channel at $Fr_1 = 2{\cdot}0$ and $h/b = 0{\cdot}5$ using various Chézy coefficients

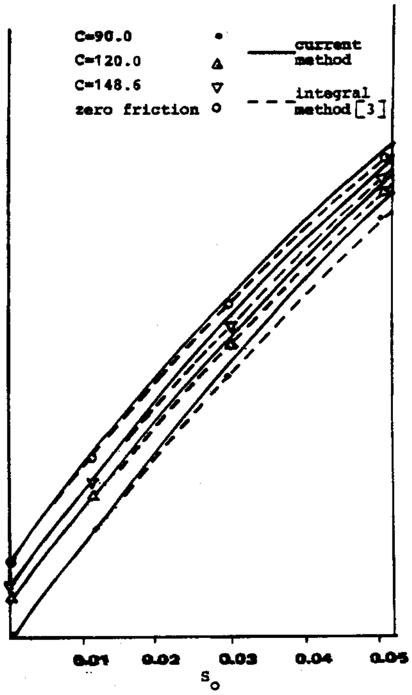

Figure 17. Predictions of exit velocity variation with Chézy's coefficient for the linearly expanding channel at $Fr_1 = 2{\cdot}0$ and $h/b = 0{\cdot}5$ using various channel slopes

Hydraulic jumps

In order to get an indication of capability of the proposed marching finite volume method to calculate hydraulic jumps, it was decided to simulate 1D flows. Thus the first test case is an H3-curve. The channel width is 5·0 m while the total length is 100·0 m. The inlet water depth is 1·150 m and the discharge is 55·4 $\mathrm{m}^3\,\mathrm{s}^{-1}$. A 2·80 m exit water depth is applied and the problem is to calculate the location and strength of the hydraulic jump when the Manning flow friction coefficient $n = 0{\cdot}020$. The standard quasi-2D fixed-step numerical method described earlier (equation (26)) was employed and the comparison of the predictions is shown in Figure 18. The agreement is satisfactory, although the exact location of the marching finite volume prediction is Δx or $2\Delta x$ downstream from that computed by the standard quasi-2D method. When an adverse slope is applied ($S_o = -0{\cdot}001$) with identical flow conditions and geometry as described for the H3-curve, except for the exit water depth which is now 2·74 m, the predicted results are as shown in Figure 19 and are considered to be satisfactory. In this case the marching finite volume result

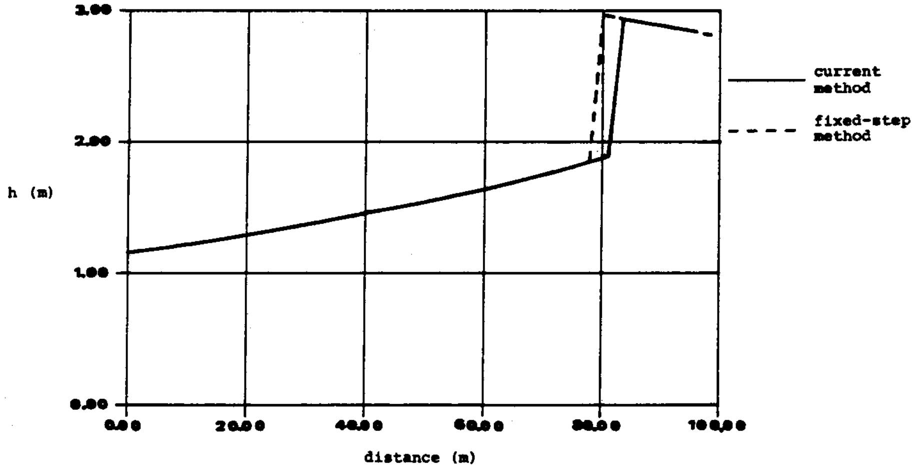

Figure 18. Hydraulic jump predictions for an H3-curve

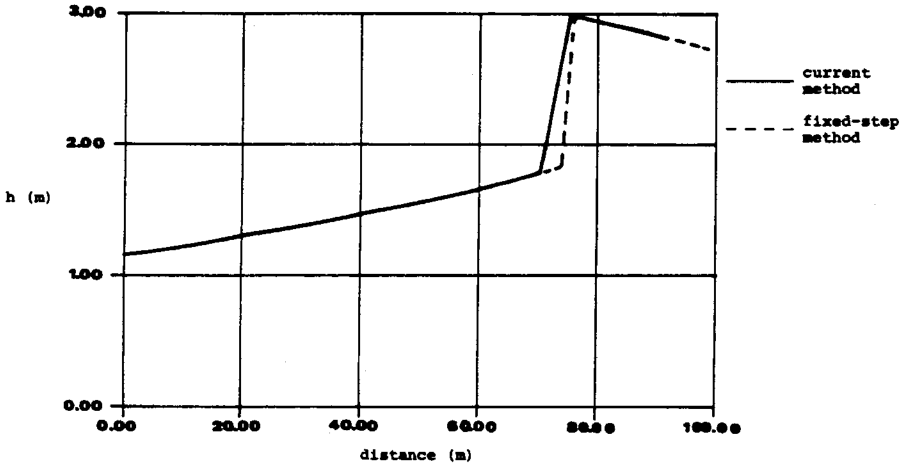

Figure 19. Hydraulic jump predictions for an A3-curve

for the location of the hydraulic jump appears to be upstream from that computed by the standard quasi-2D method.

Channel expansion at $Fr_1 = 2{\cdot}0$ after Rouse et al.[5]

The channel expansion shown in Figure 20 was used to test the accuracy of the numerical method by comparing it with the results of other numerical methods as well as with measurements. The expansion shown was designed for an entrance Froude number of 2·0.

The actual channel geometry is given by the formula

$$y/b_1 = \tfrac{1}{2}(x/2b_1)^{3/2} + \tfrac{1}{2}, \tag{27}$$

where b_1 is the channel width at entrance. Figure 20 also shows the flow depth contours h/h_1 as measured by Rouse *et al.* Comparisons between predictions and measurements for the above channel are shown in Figures 21–23 for the centreline, mid-stream line and curved side respectively. Three numerical methods are presented: an integral method,[2] an explicit two-step (predictor–corrector) scheme (McCormack)[2] and the current numerical scheme. The comparisons are considered to be satisfactory.

Channel expansion at $Fr_1 = 4{\cdot}0$ after Rouse et al.[5]

Finally, the channel expansion shown in Figure 24 was used to test the accuracy of the method for high entrance Froude number (=4·0). The actual channel geometry is now given by the formula

$$y/b_1 = \tfrac{1}{2}(x/4b_1)^{3/2} + \tfrac{1}{2}. \tag{28}$$

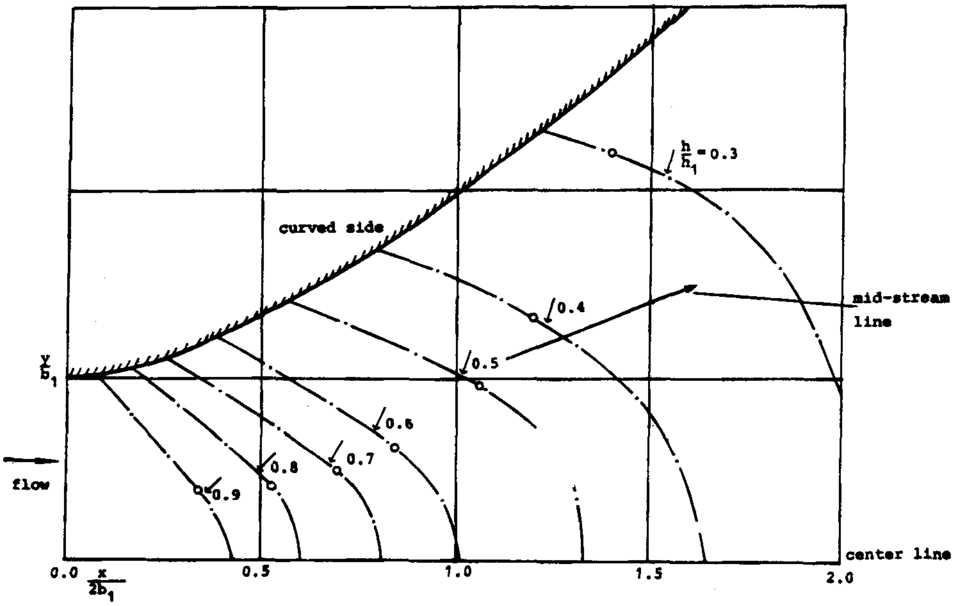

Figure 20. Channel geometry for $Fr_1 = 2{\cdot}0$ after Rouse *et al.*,[5] with measured h/h_1 contours

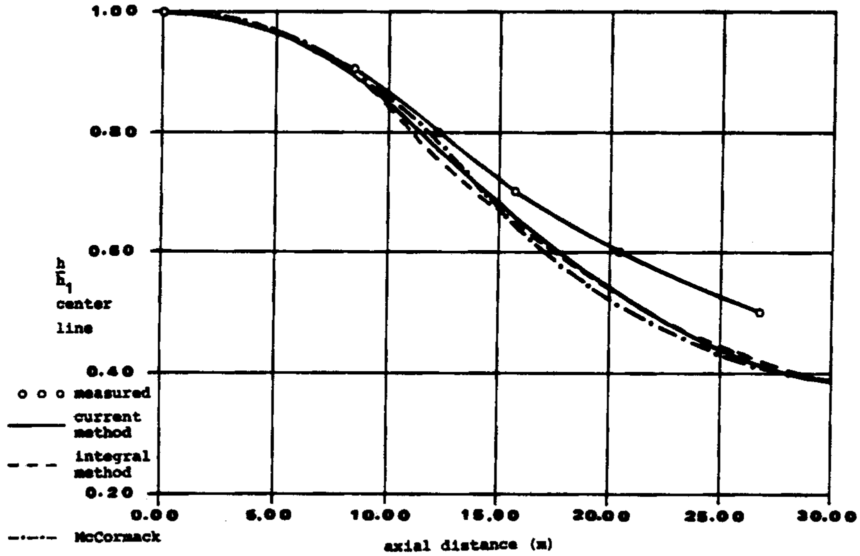

Figure 21. Comparison between predictions and measurements for the Rouse *et al.* channel (centreline) at $Fr_1=2{\cdot}0$, $S_o=0{\cdot}0$ and $n=0{\cdot}012$

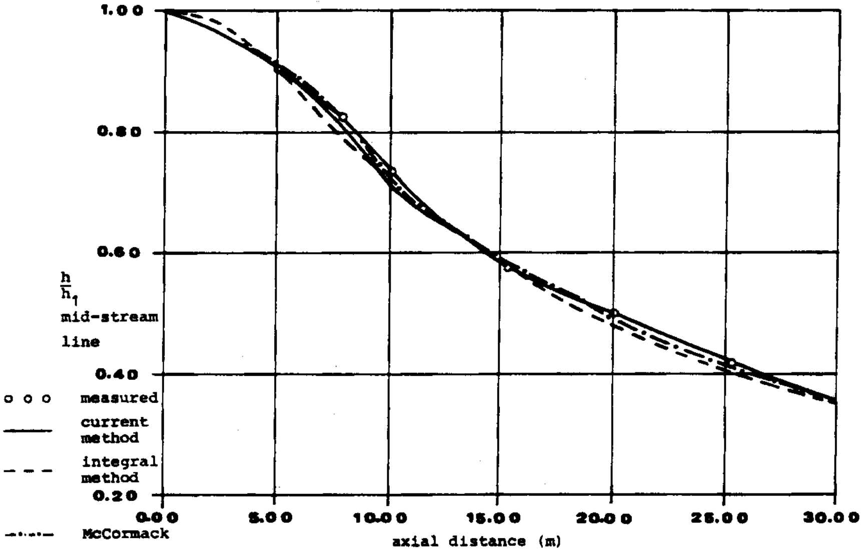

Figure 22. Comparison between predictions and measurements for the Rouse *et al.* channel (mid-stream line) at $Fr_1=2{\cdot}0$, $S_o=0{\cdot}0$ and $n=0{\cdot}012$

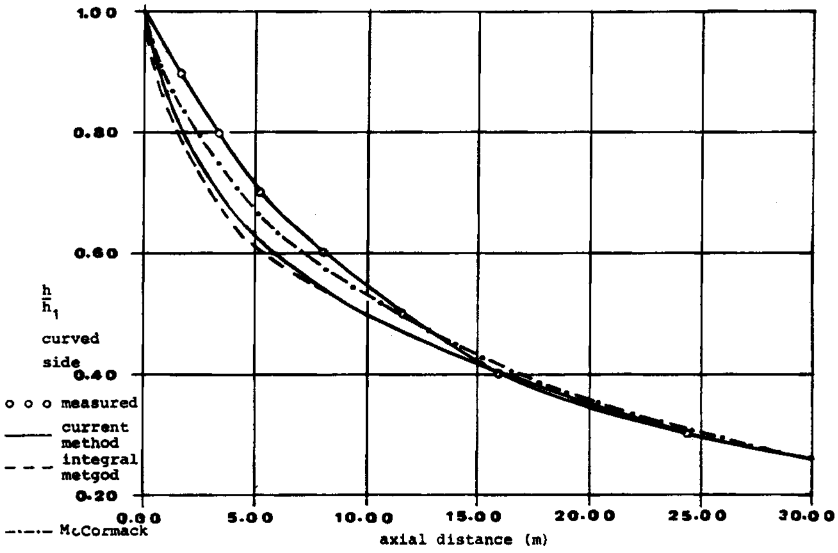

Figure 23. Comparison between predictions and measurements for the Rouse *et al.* channel (curved side) at $Fr_1=2{\cdot}0$, $S_o=0{\cdot}0$ and $n=0{\cdot}012$

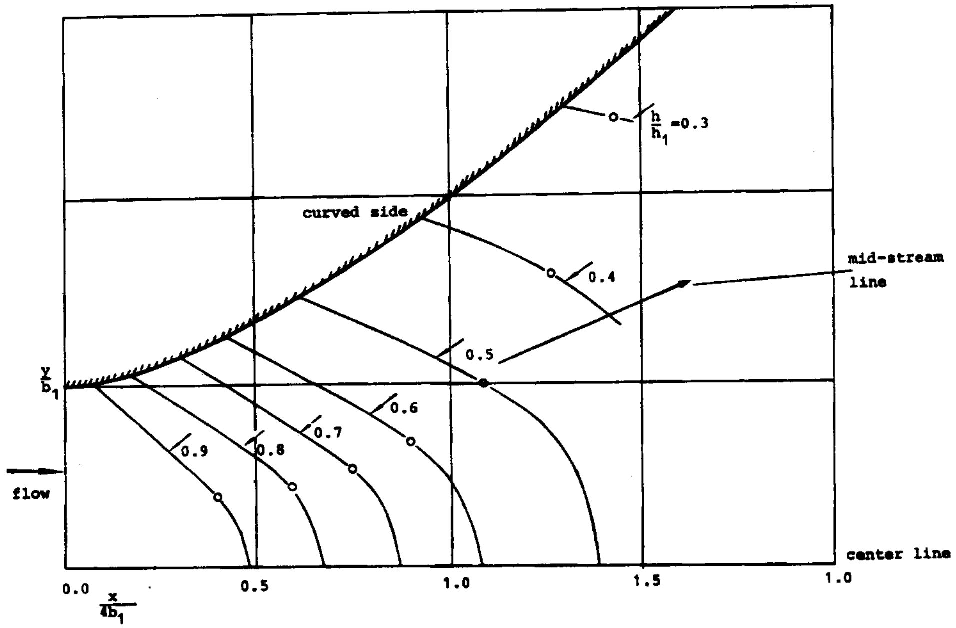

Figure 24. Channel geometry for $Fr_1=4{\cdot}0$ after Rouse *et al.*,[5] with measured h/h_1 contours

Comparisons between predictions and measurements for the above channel are shown in Figures 25–27 for the centreline, mid-stream line and curved side respectively. Again the predicted results agree with each other, while their agreement with measurements seems to be satisfactory particularly along the mid-stream flow line.

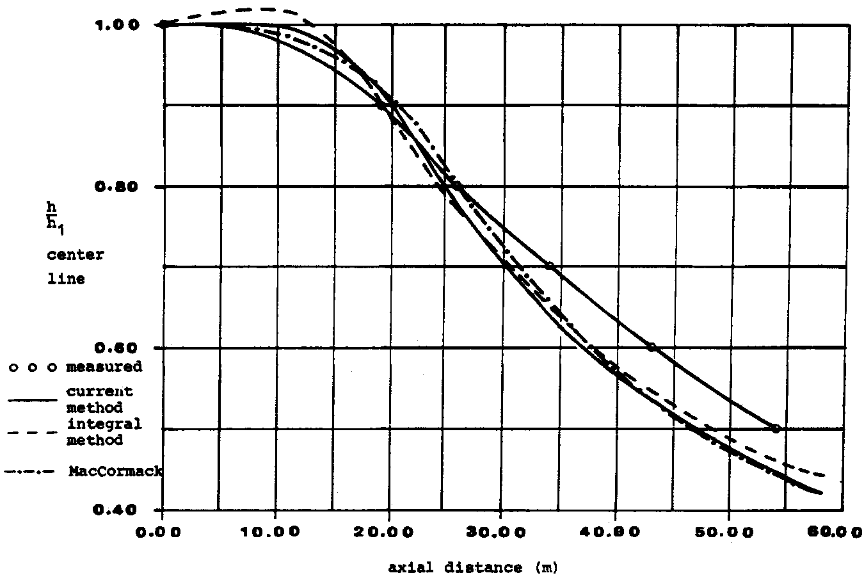

Figure 25. Comparison between predictions and measurements for the Rouse *et al.* channel (centreline) at $Fr_1=4{\cdot}0$, $S_o=0{\cdot}0$ and $n=0{\cdot}012$

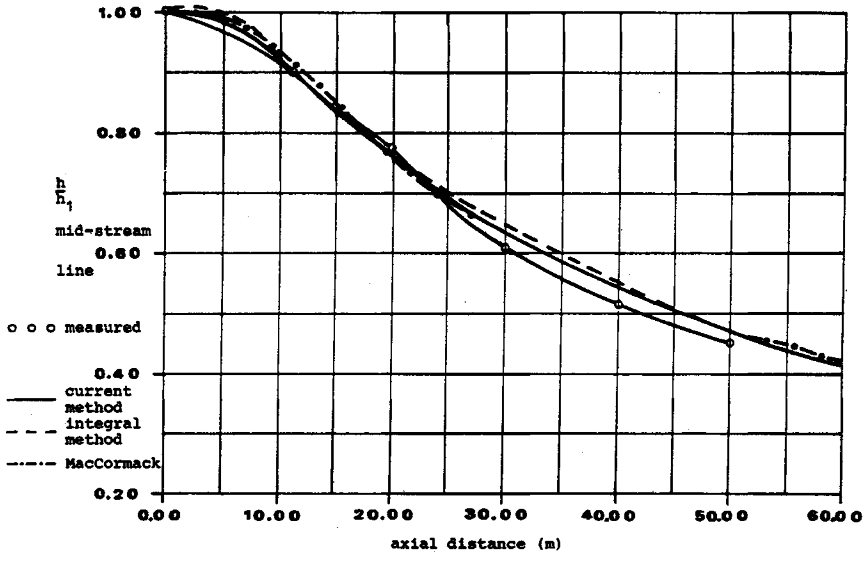

Figure 26. Comparison between predictions and measurements for the Rouse *et al.* channel (mid-stream line) at $Fr_1=4{\cdot}0$, $S_o=0{\cdot}0$ and $n=0{\cdot}012$

In order to calculate the slope effects, it was decided to test the above channel using four different slopes, namely $S_{ox}=0{\cdot}025$, $0{\cdot}050$, $0{\cdot}100$ and $0{\cdot}200$. The slope S_{oy} was kept equal to zero. The predicted results are shown in Figures 28–30 for the centreline, mid-stream line and curved side respectively. High slopes yield lower depth ratios, which is an expected result. In all three figures the flat slope solution is also presented.

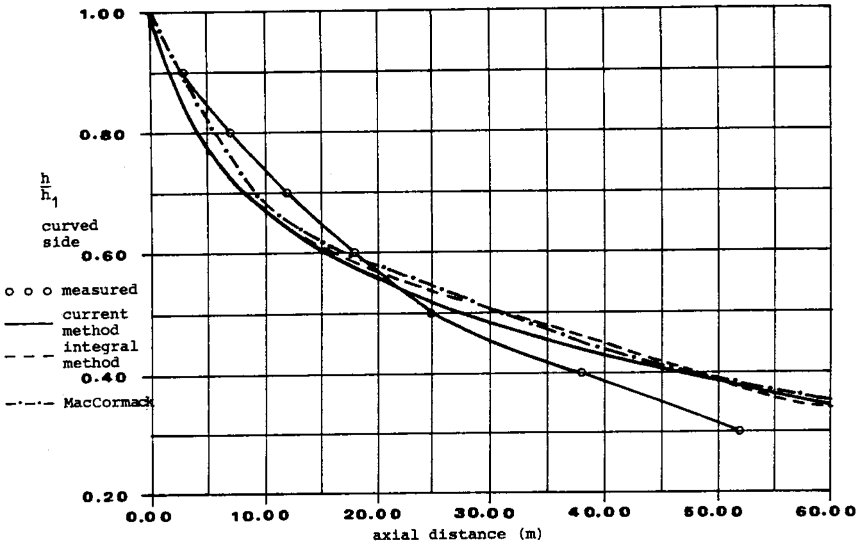

Figure 27. Comparison between predictions and measurements for the Rouse *et al.* channel (centred side) at $Fr_1 = 4{\cdot}0$, $S_o = 0{\cdot}0$ and $n = 0{\cdot}012$

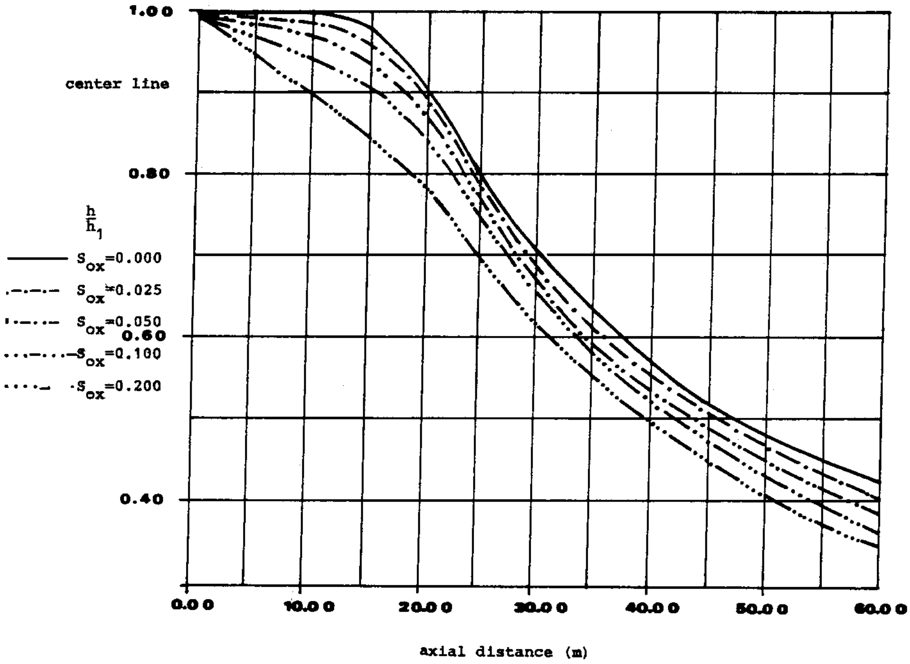

Figure 28. Computed results for the Rouse *et al.* channel (centreline) at $Fr_1 = 4{\cdot}0$, $S_{oy} = 0{\cdot}0$ and $n = 0{\cdot}012$ using various bottom slopes

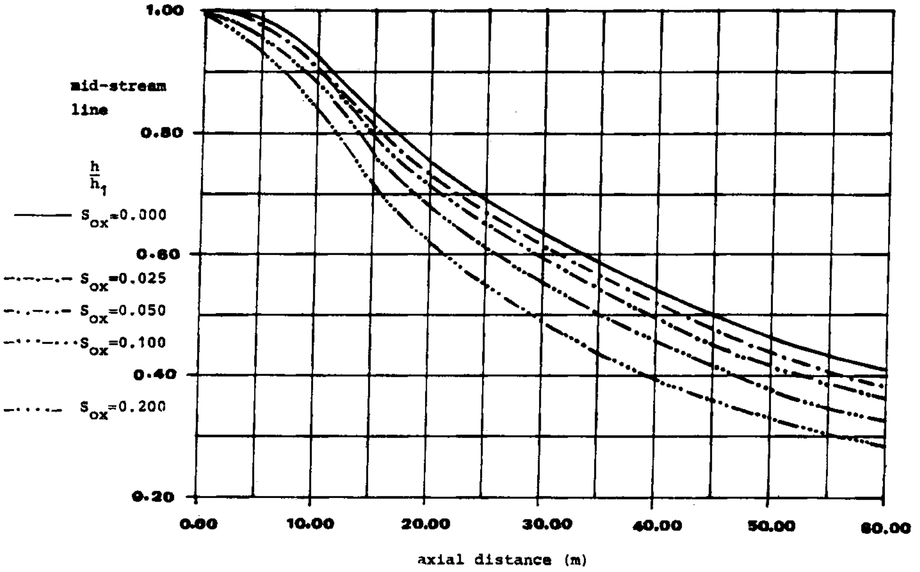

Figure 29. Computed results for the Rouse *et al.* channel (mid-stream line) at $Fr_1=4{\cdot}0$, $S_{oy}=0{\cdot}0$ and $n=0{\cdot}012$ using various bottom slopes

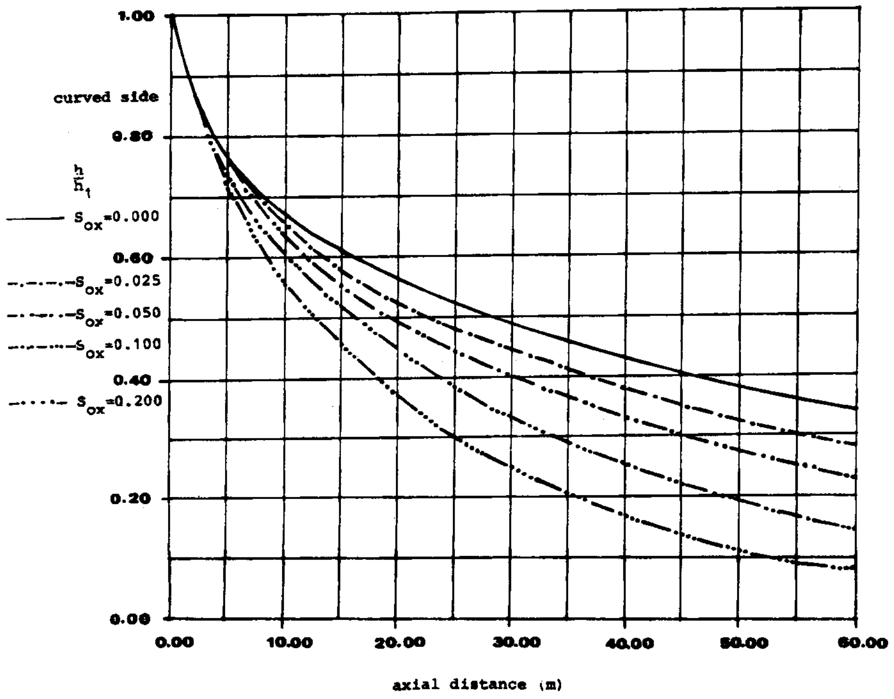

Figure 30. Computed results for the Rouse *et al.* channel (curved side) at $Fr_1=4{\cdot}0$, $S_{oy}=0{\cdot}0$ and $n=0{\cdot}012$ using various bottom slopes

The Froude number distributions along the axial distance for the centreline, mid-stream line and curved side of the channel are shown in Figure 31. In nearly all regions the flow is expanding. However, in the first 20% of the axial distance and along the centreline the Froude number is slightly lower than the initial inlet one set forth. The variation of the centreline exit Froude number distribution with the entrance Froude number is shown in Figure 32. A flat slope was used

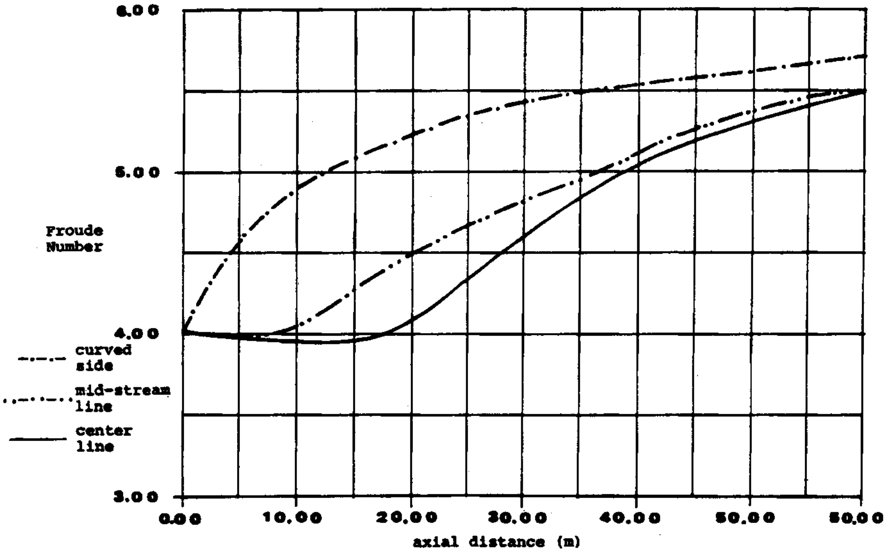

Figure 31. Froude number predictions for the Rouse *et al.* channel at $Fr_1=4{\cdot}0$, $S_{ox}=0{\cdot}0$ and $n=0{\cdot}012$

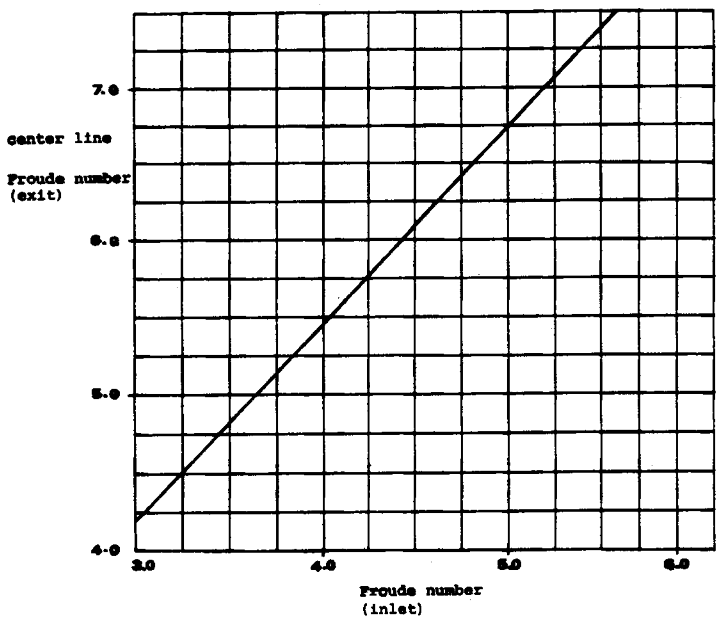

Figure 32. Predicted exit Froude number distribution for the Rouse *et al.* channel ($Fr_1=4{\cdot}0$ design) at $n=0{\cdot}012$ and $S_o=0{\cdot}0$ using variable entrance flow

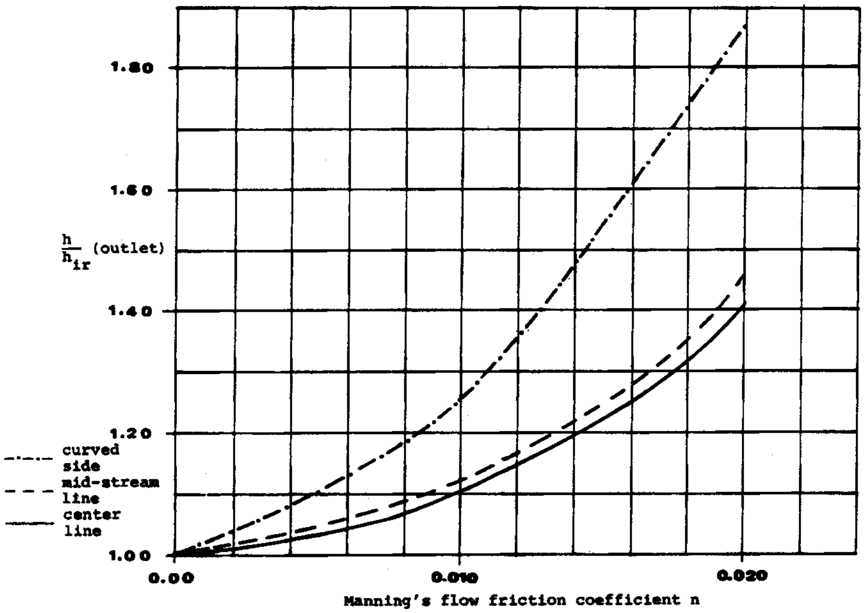

Figure 33. Predicted flow friction effects for the Rouse *et al.* channel at $Fr_1 = 4{\cdot}0$ and $S_{ox} = 0{\cdot}0$

along with a Manning flow friction coefficient n of 0·012. Finally, the effects of using various friction coefficients on the h/h_{ir} ratio for $Fr_1 = 4{\cdot}0$ and a flat slope are shown in Figure 33. Again, higher friction resulted in higher h/h_{ir} depth ratios. This behaviour is the expected one.

CONCLUSIONS

A marching finite volume numerical method has been developed and subsequently applied to open channel flow calculations. There are two main advantages of the method. The first is the ability to calculate subcritical–supercritical types of flow. The second is the utilization of a body-fitted non-orthogonal local co-ordinate system. Thus the developed algorithm is able to calculate two-dimensional, steady, subcritical and/or supercritical flows including the usually neglected terms of slope and bottom friction. The method has been applied to a variety of open channel flow configurations in order to validate its potentialities. The applications include: subcritical flow in a straight parallel wall channel; convex chute in converging supercritical flow; linearly expanding channel; hydraulic jumps; channel expansions designed at specific entrance Froude numbers ($Fr_1 = 2{\cdot}0$ and 4·0). Comparisons with available measurements and/or other numerical solutions show that the proposed method is comparatively accurate, reliable and fast. It can be extended to the design of spillway chutes in order to obtain the desired flow depth distribution.

REFERENCES

1. J. D. Denton, 'An improved time-marching method for turbomachinery flow calculation', *ASME Paper 82-GT-239*, 1982.
2. J. V. Soulis and K. V. Bellos, 'Steady, supercritical, open channel flow computations', *Proc. 6th Int. Conf. on Numerical Methods in Laminar and Turbulent Flow*, Swansea, 11–15 July 1989. Pineridge Press, 1989, pp. 1493–1504.

3. J. V. Soulis, 'Two-dimensional high-speed, open channel flow friction effects', *Int. Conf. on Channel Flow and Catchment Runoff: Centennial of Manning's Formula and Kuichling's Rational Formula*, University of Virginia, Charlottesville, VA, 22–26 May 1989.
4. A. Ippen, 'Mechanics of supercritical flow', *Trans. ASCE*, **116**, 268–295 (1951).
5. H. Rouse, B. V. Bhoota and En-Yen Hsu, 'Design of channel expansions', *Trans. ASCE*, **116**, 347–363 (1951).
6. A. Ippen and J. H. Dawson, 'Design of supercritical contractions', *Trans. ASCE*, **116**, 326 (1951).
7. J. A. Liggett and S. U. Vasudev, 'Slope and friction effects in two-dimensional high speed channel flow', *International Association for Hydraulic Research 11th Int. Congr.*, Leningrad, 1965.
8. J. J. McGuirk and W. Rodi, 'A depth-averaged mathematical model for the nearfield of side discharges into open channel flow', *J. Fluid Mech.*, **86**, 761–781 (1978).
9. R. S. Chapman and C. Y. Kuo, 'Application of high accuracy finite-difference technique to steady free surface flow problems', *Int. j. numer. methods fluids*, **3**, 583–590 (1983).
10. R. S. Chapman and C. Y. Kuo, 'Application of the two equation k–ε turbulence model to a two-dimensional, steady, free-surface flow problem with separation', *Int. j. numer. methods fluids*, **5**, 257–268 (1985).
11. A. O. Demuren, 'Numerical computation of supercritical and subcritical flows in open channels with varying cross-sections', *Finite Elements in Water Resources, Proc. 4th Int. Conf.*, Hannover, June 1982. Computational Mechanics Center, Southampton, pp. 4.13–4.23.
12. D. B. Spalding, 'A general computer program for two dimensional parabolic phenomena', *HMT Series 1*, Pergamon, Oxford, 1978.
13. J. B. Herbich and P. Walsh, 'Supercritical flow in rectangular expansions', *J. Hydraul. Res. Div., Proc. ASCE*, **100**, 553–568 (1972).
14. J. L. Steger, 'Implicit finite-difference simulation of flow about arbitrary two-dimensional geometries', *AIAA J.*, **16**, 679–686 (1978).
15. K. V. Bellos, J. V. Soulis and J. G. Sakkas, 'Computing 2D unsteady open channel flow by finite-volume method', *VII Int. Conf. on Computational Methods in Water Resources*, MIT, 13–17 June 1988. Computational Mechanics Publications, Southampton, pp. 357–362.
16. J. V. Soulis and K. V. Bellos, 'Conservation form of fluid dynamics equations in curvilinear coordinate systems. Part I: Mathematical analysis', *Tech. Chron. Section. B.* **8**, (4), 69–97 (1988).
17. F. M. Neilson, 'Convex chutes in converging supercritical flow', *U.S. Army Engineer Waterways Experiment Station, Miscellaneous Paper 17-76-19*, September 1976.